https://doi.org/10.1016/j.electacta.2021.138135

AZ31 magnesium alloy with ultrafine grains as the anode for Mg-air battery

Naiguang Wang[a], Yixiang Huang[a], Jingjing Liu[a], Xusheng Yang[b], Weipeng Xie[a], Qiong Cai[c*], Songyuan Zheng[d], Zhicong Shi[a*]

a. School of Materials and Energy, Guangdong University of Technology, Guangzhou, 510006, China.

b. Department of Industrial and Systems Engineering, The Hong Kong Polytechnic University, Hung Hom, Kowloon, Hong Kong, China

c. Department of Chemical and Process Engineering, University of Surrey, Guildford GU2 7XH, UK

d. Shenzhen Sea Energy Power Holdings Co., Ltd, Shenzhen, 518110, China

Abstract: Fabricating the magnesium alloy with fine grains, low dislocation density, and weak grain orientation is of crucial importance to enhance its anode performance for primary aqueous battery. However, this structure mode can hardly be realized for bulk magnesium alloy via the conventional approaches such as plastic working. Herein, we construct an AZ31 magnesium alloy with ultrafine grains (667.28 ± 291.35 nm) by using the spark plasma sintering of the alloy powder that has been treated via high-energy ball milling. This alloy exhibits weak grain orientation and its dislocation density is not increased compared to the precursor alloy. Benefiting from the unique microstructure, the modified AZ31 displays significantly more active behaviour with enhanced capacity during the discharge of Mg-air battery, as compared to the precursor AZ31 that has the grain size of 472.89 ± 154.31 μm. Furthermore, the impact of ultrafine grains on the discharge behaviour is also analysed

---

*Corresponding author. Tel: +86 18933958027; Fax: + 86 020 39322570;
E-mail: wangnaiguang505@163.com (Naiguang Wang); q.cai@surrey.ac.uk (Qiong Cai); zhicong@gdut.edu.cn (Zhicong Shi)

based on microstructure characterization and electrochemical response.

Keywords: AZ31 magnesium anode; Ultrafine grains; Discharge behaviour; Mg-air battery.

1. Introduction

Metal-air batteries rely on active metals to serve as the anodes, which offer electrons for power generation whilst oxygen at the cathodes acquires these electrons via reduction reaction. Magnesium is a promising anode material owing to its negative standard electrode potential (−2.37 V (vs. SHE)) and large Faradaic capacity (2.2 A h g^{-1}) [1]. However, the oxidation products ($Mg(OH)_2$) attached to the anode surface decrease the reaction area of magnesium, thus causing the attenuation of voltage with elapsed time [2]. The inherently negative difference effect (NDE) of magnesium results in the side hydrogen evolution (i.e., self-discharge) [3, 4], and some metal particles fall off the surface of magnesium within the discharge period (chunk effect) [5]. These factors combine to make the actual capacity of Mg-air battery significantly lower than its theoretical value.

Adding alloying elements (such as Al, Zn, In, Mn, Ga, Pb, and rare earths) to magnesium is an effective means to improve its anode performance [2, 5-8], since these elements not only accelerate the exfoliation of oxidation products and restore activity, but also mitigate self-discharge and chunk effect. On the basis of compositional optimization, plastic working such as extrusion and rolling is normally adopted to refine the grain size of magnesium alloy, which is another important factor that controls its discharge performance. It is generally believed that the fine grains play a vital role in enhancing the discharge activity of magnesium anode [1, 9, 10]. However, the grain sizes of entire bulk magnesium alloys can hardly be refined bellow 1 μm (ultrafine grains) by using conventional plastic working [1, 2, 11], owing to the hexagonal structure of magnesium that worsens its plasticity

at room temperature. As a result, the working process must be implemented at elevated temperature and the grain refinement is thus hampered because of grain growth.

Additionally, the effect of fine grains on the discharge and corrosion behaviour of magnesium anode still remains controversial. Zheng *et al*. [12] suggested that raising the extrusion temperature from 180 to 250□ led to the grain growth of pure magnesium from 20 to 30 μm, thus leading to the boost of discharge activity and the rise in corrosion current density. Cui *et al*. [10] reported that the fine-grained microstructure in Mg-Al-Pb-Ga-Y anode increased the density of grain boundaries and the number of second phases along the grain boundaries, therefore promoting its corrosion rate and discharge activity. According to Liu *et al*. [13], the smaller grains induced by extrusion can improve the corrosion resistance of Mg-Al-Zn-Ca-RE anode. One of the interference factors responsible for this controversy is the second phases in magnesium alloys; the discontinuous distribution of second phases along the grain boundaries strengthen the micro-galvanic effect and accelerate the corrosion of surrounding matrix [10].

Dislocations and texture (grain preferred orientation) in bulk magnesium alloys produced by plastic working also interfere with the revealing of fine grains effect on their discharge and corrosion behaviour. High density of dislocations can accelerate the formation of $Mg(OH)_2$ and promote the self-corrosion [14], while the influence of grain preferred orientation is relatively more complicated. Previous work demonstrated that (0001) basal texture strengthened the corrosion resistance of AP65 magnesium alloy at open circuit potential (OCP) but weakened its activity during discharge, whereas (10−10) and (11−20) grain orientations were able to improve the discharge activity but debased the corrosion resistance at OCP [15]. Hence, new methods are needed to construct the magnesium alloy with fine grains, low dislocation density, and weak preferred orientation for elucidating the influence

of fine grains on the discharge and corrosion behaviour, along with boosting its anode performance.

In this work, we fabricate the AZ31 magnesium anode with ultrafine grains by using the spark plasma sintering of the alloy powder that has been treated through high-energy ball milling at room temperature. The process of ball milling can create nanocrystals in the alloy powder [16, 17], while the spark plasma sintering mitigates the grain growth due to its rapid heating rate and short sintering period [18]. To our knowledge, this is the first time that the bulk metal anodes with ultrafine grains (< 1 μm) are used in primary aqueous batteries. Moreover, the dispersion of nanoscale Al_3Mn phase is achieved as akin to the precursor AZ31 ingot; the dislocation density along with grain orientation intensity are not increased after sintering. The aim of this work is to construct the magnesium anode with fine grains, low dislocation density, and weak grain orientation for improving its performance. Benefiting from the unique microstructure, interference factors such as dislocations, grain preferred orientations, and second phases along the grain boundaries are eliminated, contributing to unveiling of the correlation between ultrafine grains and discharge behaviour for AZ31 magnesium anode.

2. Experiments

2.1 Synthesis of material

The process of material synthesis was schematically shown in Fig. 1. The as-cast AZ31 alloy (Mg-3.1 wt.% Al-1.0 wt.% Zn-0.2 wt.% Mn) was purchased from Chongqing Yuhua New Material Technology Co., Ltd., China. It was homogenized at 400□ for 24 h followed by water quenching to act as the precursor alloy (denoted as H), of which the drill cuttings were produced in a glovebox (MIKROUNA) by using an electric drill. These drill cuttings were then treated with a high-energy ball mill (FRITSCH) at room temperature using zirconia jar and balls to prepare the alloy powder.

The mass ratio of ball to material was 15:1, and the ball milling speed along with the milling time were 300 rpm and 20 h, respectively. The average size of the milled alloy powder was 29.68 ± 8.23 μm; its relative homogeneity could be ensured with the homogenization treatment. Thereafter, the milled alloy powder was put into a pure graphite mould and prepressed by hand, and then the mould along with the powder were placed in a spark plasma sintering furnace (Dr. Sinter model SPS-825) to produce the bulk alloy with a dimension of Φ20 mm × 25 mm (named as SPS). The pressure was 30 MPa and the sintering temperature was raised to 400□ with a rate of 80□ min^{-1}. The holding period at 400□ was 5 min and the sintered ingot with a relative density of 99.9% was cooled down to room temperature within the furnace.

[Insert Fig. 1 here]

2.2 Microstructure characterization

The X-ray diffraction spectra of H and SPS were measured by using an X-ray diffractometer (XRD; D/MAX-Ultima IV) with Cu Kα radiation. The 2θ was scanned from 20 to 80° at 2° min^{-1}. An optical microscope (OM; XJP-6A) was used to reveal the grain size of H, which had been ground with SiC abrasive paper and polished through diamond paste, and then etched with a solution of 70 ml deionized water, 1 ml nitric acid, 1 ml acetic acid, and 1 g oxalic acid. The microstructure details of both H and SPS were observed via a transmission electron microscope (TEM; FEI Talos F200X); the samples before TEM tests had been ground to a thickness of 0.1 mm and then subjected to Ar^+ ion-milling.

2.3 Electrochemical measurement

A CHI750E electrochemistry workstation equipped with a classic three-electrode system were adopted to monitor the discharge and corrosion behaviour of H and SPS, which acted as the working electrodes. Prior to electrochemical testing, the surfaces of H and SPS were polished via 1200 grade SiC abrasive paper. The counter and the reference electrodes were a platinum slice and a saturated calomel electrode (SCE), respectively. The electrolyte was 3.5 wt.% NaCl aqueous solution and the tested area for each working electrode was 10 mm × 10 mm. The polarization curves were recorded by scanning the potential from −1.9 V (vs. SCE) in anodic direction at 1 mV s^{-1}. The electrochemical impedance spectra (EIS) were measured at OCPs after the tested samples had been immersed in the electrolyte for 5 min. The amplitude was 5 mV and the frequency varied from 10^5 to 0.05 Hz. Zview software was then employed to fit these EIS data. The evolved hydrogen at OCPs and in the course of galvanostatic discharge was collected via a beaker and a burette that were filled with electrolyte. The time for collecting the hydrogen at OCPs and during galvanostatic discharge was 72 h and 180 min, respectively. Figure 2 showed the schematics of measuring the hydrogen volume in the course of discharge.

[Insert Fig. 2 here]

The discharge performance of Mg-air batteries with H and SPS anodes was evaluated based on a LANHE-CT2001A battery testing system. The electrolyte was 3.5 wt.% NaCl aqueous solution and the cathode was a commercial air electrode with MnO_2/C catalyst. The cell voltages at 10 and 20 mA cm^{-2} were monitored by galvanostatic discharge, and the anodic efficiencies along with the battery capacities were calculated according to Faraday's law and mass loss method [1, 5]. Chromic acid was adopted to remove the oxidation products, and the corroded surfaces with and without the oxidation products were observed via a scanning electron microscope (SEM; S-3400). To reflect the

degree of uniform dissolution during long period of discharge, a laser scanning confocal microscope (Olympus OLS4000) was employed for testing the three-dimensional morphologies of the corroded surfaces after cleaning the oxidation products.

All electrochemical experiments were carried out at room temperature and repeated three times to ascertain the reproducibility of data.

3. Results and discussion

3.1 Microstructures

The XRD spectra shown in Fig. 3(a) indicate that both H and SPS exhibit only α-Mg, attributed to the low contents of alloying elements that cannot be detected via XRD. The (10−10) peak in SPS is obviously lower than that in H; many peaks that cannot be clearly identified in H, such as (0002), (10−12), (11−20), and (11−22), are all distinct in SPS. As a consequence, high-energy ball milling and spark plasma sintering create random grain orientations in AZ31 and the texture intensity is thus not improved. The optical micrograph displayed in Fig. 3(b) reveals the equiaxed grains in H, and the linear intercept method manifests the normal distribution of the grain sizes with an average value of 472.89 ± 154.31 μm, as given in Fig. 3(c). Five images with the same magnification of Fig. 3(b) at different areas are employed to obtain the grain size distribution and the average grain size of H. The TEM images (Fig. 3(d)-(e)) unveil that H exhibits low density of dislocations and the nanoscale second phase particles are dispersed well in its matrix. The high-resolution (HR) TEM image (Fig. 3(f)) provides the microstructure details of the second phase, which is hereafter identified as Al_3Mn phase with the assistance of Fourier transform (FFT) (inset in Fig. 3(e)) and Energy-dispersive X-ray spectroscopic (EDX) analysis (Fig. 3(k)).

[Insert Fig. 3 here]

According to the TEM images shown in Fig. 3(g), SPS also exhibits equiaxed grains and their sizes are significantly refined compared with those of H. The density of dislocations in SPS is also low, and the nanoscale particles still remain a homogeneous distribution in the matrix, as confirmed by the magnified image given in Fig. 3(h). The HR TEM image (Fig. 3(i)), FFT result (inset in Fig. 3(h)), and EDX analysis (Fig. 3(l)) show that these particles are Al_3Mn, attesting no phase-transition in the course of high-energy ball milling and spark plasma sintering. Four images at different areas with the same magnification of Fig. 3 (g) are employed to measure the grain sizes, and the statistical analysis shows that the average grain size of SPS is 667.28 ± 291.35 nm (Fig. 3(j)), which is smaller than those of bulk AZ31 magnesium alloys underwent severe plastic deformation and high densities of dislocations also exist in these alloys [19-21]. In this work, the unique microstructure of SPS is caused by the joint effect of high-energy ball milling and spark plasma sintering. The former could produce nanocrystals and crystal deficiencies in magnesium alloy powder due to the strong impact of zirconia balls at room temperature [22], while the latter is able to suppress the grain growth to some degree owing to the short sintering time (5 min). However, recrystallization still occurs during sintering and conduces to the decrease in dislocation density and the formation of equiaxed grains, as the sintering temperature (400□) is higher than the recrystallization temperature of magnesium (~250□).

3.2 Electrochemical discharge behaviour

The polarization curves shown in Fig. 4(a) indicate that SPS exhibits more negative corrosion potential than H, which possesses smaller absolute value of cathodic Tafel slope (−113.7 mV dec^{-1}).

Since the cathodic branch is associated with hydrogen evolution, the larger absolute value of slope (-145.5 mV dec^{-1}) indicates that SPS displays sluggish kinetics for the evolution of hydrogen during cathodic polarization. According to the microstructure characterization presented in Fig. 3, both H and SPS have low density of dislocations, and the nanoscale Al_3Mn particles are dispersed well in their matrix. Thus, the electrochemical response of the two specimens is mainly related to the grain sizes. Compared to H with micro-sized grains, the ultrafine grains in SPS produce significantly more grain boundaries, which can act as the local anodes owing to the crystal defects that make the grain boundaries more active than the regions inside the grains (local cathodes) [23]. Accordingly, smaller ratio of local cathodes/anodes is established in SPS and mitigate the evolved hydrogen when applied cathodic polarization, as compared with H possessing larger ratio of local cathodes/anodes. This suppressive effect for hydrogen evolution will be further discussed during battery discharge.

[Insert Fig. 4 here]

In addition to the cathodic branches, the two specimens also exhibit different electrochemical behaviour during anodic polarization, which is related to the dissolution of working electrodes. The anodic branch of H undergoes two-stage profiles with different slopes (77.5 and 62.4 mV dec^{-1}), of which the intersection is the indication of breakdown for the oxidation products. By contrast, SPS shows only one stage in the whole anodic branch, and its slope (25.7 mV dec^{-1}) is obviously smaller than those of H and most of magnesium alloys [1, 2, 6, 24]. Hence, the kinetics of anodic dissolution is greatly accelerated for SPS since its ultrafine grains construct a large number of grain boundaries, which possess more crystal deficiencies and could provide the channels for reaction [23]. The effect of ultrafine grains on the anodic behaviour will be further analysed based on battery discharge.

Figure 4(b) gives the corrosion current densities (J_{corr}) and corrosion potentials (E_{corr}) evaluated

from the polarization curves. The J_{corr} is calculated by extrapolating the linear cathodic branch back to the E_{corr}. It can be seen that SPS has significantly larger J_{corr} than H, and this result is consistent with the EIS at OCPs (Fig. 4(c)). The obvious shrinkage in EIS and larger J_{corr} demonstrate the more active behaviour of SPS at OCP. According to Kim *et al*. [25], the increased grain boundary densities may enhance overall surface reactivity and hence produce a significant corrosion rate of SPS. The equivalent circuits depicted in Fig. 4(e) are adopted to fit these EIS. For the two circuits, R_{ct} is the resistance of charge transfer that occurs at the electrode/electrolyte interface (electric double layer), and C_{dl} is the capacitance of electric double layer. Because the electrode is covered by surface film, the parallel connection of C_{dl} and R_{ct} is in series with R_{pore}, which is the resistance for the electrolyte ions penetrating through the pores of surface film. The three elements are parallel connected with CPE_f that is the constant phase element reflecting the inhomogeneity of surface film. The left circuit model is also employed by Li *et al*.[3]. Since the inductive loop for SPS is caused by the dissolution of surface film [26], R_L and L (inductance) in the right circuit is in parallel with CPE_f, R_{pore}, R_{ct}, and C_{dl} to express that the dissolution of film and charge transfer process occur within the whole surface film. According to Fig. 3, grain size is the main difference between H and SPS; thus, the accelerated dissolution of surface film is related to the large number of grain boundaries in SPS created by its ultrafine grains. Moreover, no inductive loop appears in the EIS of H sample, and this phenomenon is different from the EIS of AZ31 in several literature studies [27, 28]. The probable reason might be the preparation conditions such as casting, heat treatment, and plastic deformation that influence the microstructure features and thus induce different EIS response. Table 1 lists the fitted results of EIS; both the two curves are fitted well with low values of χ^2, and the R_f along with R_{ct} of H are obviously larger than those of SPS, respectively. Hence, H is protected well by the surface film and

dissolves slowly, rendering it corrosion-resistant at OCP.

[Insert Table 1 here]

To confirm the electrochemical testing, the evolved hydrogen without applying any current is collected and the gas volumes could reflect the dissolution of tested samples at OCPs. According to Fig. 4(d), H releases obviously less hydrogen than SPS after immersion for 72 h. As a consequence, the ultrafine grains promote the active dissolution of SPS at OCPs, attributed to its large number of grain boundaries that are favourable to the breakdown of surface oxidation film. This conclusion is different from the investigation of Parfenov *et al*. [29] who found the improved corrosion resistance of ultrafine-grained Mg-Ca alloy. The continuous nano-precipitation of Mg_2Ca was formed with the assistance of ultrafine grains, favouring the formation of surface protective film. The small amount of Mg_2Ca along the grain boundaries can make the alloy less susceptible to corrosion propagation. Herein, both H and SPS exhibit similar morphologies of Al_3Mn particles, which are dispersed well in the matrices and hence the corrosion behaviour is mainly controlled by the grain sizes. Since the Mg-air battery could be stored in dry places before putting into use, the high corrosion rate of anode at OCP does not cause problems.

Figure 5 displays the anode performance of H and SPS during the discharge of Mg-air batteries. SPS has higher voltages than H at 10 and 20 mA cm^{-2}, as presented in Fig. 5(a) and (b), respectively. The average voltages discharged for 10 h are listed in Table 2; the voltage of SPS at 10 mA cm^{-2} is 1.211 ± 0.004 V, which is higher than that of H. Additionally, voltage attenuation is obvious for H with prolonged time at 20 mA cm^{-2}, whereas SPS maintains relatively stable voltages at both current densities. According to Fig. 6(a) and (c), the oxidation products on the surfaces of H have relatively fewer cracks, suggesting that the electrolyte cannot be in full contact with the electrode surface. In

contrast, obviously more cracks are observed on the surfaces of SPS (Fig. 6(b) and (d)), and hence the spalling of oxidation products is promoted during discharge. Thus, SPS maintains large reaction surface regions that contribute to its stable and high cell voltages. Since the two specimens exhibit negligible difference in the dislocation densities, grain orientations, and second phases (Fig. 3), their different discharge behaviour is originated from grain sizes. The ultrafine grains in SPS can create significantly more grain boundaries than H that has micron-scale grains; these grain boundaries with more crystal defects possess high energy [23, 24], thus acting as the channels for dissolution reaction and promoting the kinetics of anodic dissolution. Moreover, huge number of cracks on the corroded surfaces also indicate that the ultrafine grains in SPS are conducive to the dissolution of oxidation products in the course of discharge, as consistent with the inductive loop in the EIS (Fig. 4(c)). All these factors are responsible for the stronger discharge activity of SPS compared with H.

[Insert Fig. 5 here]

[Insert Table 2 here]

[Insert Fig. 6 here]

The representative hydrogen evolution behaviour of the two specimens discharged at 10 and 20 mA cm^{-2} is shown in Fig. 5(c) and (d), respectively. The same experiment is repeated for three times and the deviation of hydrogen volumes among the parallel measurements is lower than 0.3 ml cm^{-2} for 3 h testing. It can be observed that H releases larger volumes of hydrogen at both current densities, whereas the bubble evolution is effectively inhibited for SPS. This is different from what happens at OCPs when the evolution of hydrogen for SPS is more severe than that for H (Fig. 4(d)). The different hydrogen evolution behaviour with H and SPS is attributed to the surface state affected by the impressed current, which promotes the dissolution of initial protective film formed at OCPs.

As a consequence, the fresh surfaces of SPS and H are exposed to electrolyte and subjected to active corrosion.

Under this condition, the grain boundaries with strong activity serve as the local anodic areas, whilst the intragranular areas with lower energy act as the local cathodes. Therefore, micro-galvanic couple is established in the two samples, and the grain boundaries dissolve more quickly in contrast with the intragranular regions, which are the main places for severe gas evolution during discharge. This mechanism is schematically depicted in Fig. 6(e) and (f), in which the red and green arrows represent the dissolution of magnesium and the evolution of hydrogen, respectively, and the arrow length denotes the intensity of one reaction. The fewer grain boundaries in H can construct the large ratio of local cathodes/anodes, whereas SPS with significantly more grain boundaries enables the formation of small cathodes/anodes ratio. Thereby, hydrogen evolution is alleviated in SPS while H with large ratio of local cathodes/anodes releases more hydrogen during discharge. Additionally, the Al_3Mn phase with obviously higher potential than the magnesium matrix [30] can also serve as the local cathode to accelerate the evolution of hydrogen and the dissolution of surrounding magnesium matrix. However, both SPS and H show similar morphologies and distributions of Al_3Mn (Fig. 3); accordingly, the difference in anodic dissolution and hydrogen evolution behaviour between the two samples is mainly caused by the different grain sizes, not Al_3Mn phase. Figure 6(a)-(d) shows that the oxidation products of both SPS and H are not integrated but exhibit cracks, which result in the catalytic activity of NDE and the evolution of hydrogen will not be inhibited with elapsed time [31]. Table 3 gives the hydrogen evolution rates at different conditions; the NDE of magnesium makes the rate increase with increasing current density, and SPS has lower hydrogen evolution rate than E21, WE43, AM50, and ZE41 magnesium alloys [32] at 10 mA cm^{-2}. Because of the advantage in

mitigating the parasitic side reaction, SPS with strong discharge activity is a good candidate for the anode of Mg-air battery.

[Insert Table 3 here]

The anodic efficiencies and capacities during galvanostatic discharge are displayed in Fig. 5(e) and (f), respectively. SPS provides higher efficiencies and capacities than H at both 10 and 20 mA cm^{-2}. The capacity of SPS at 10 mA cm^{-2} is 1530 ± 20 mA h g^{-1}, and the corresponding efficiency reaches 69.1 ± 0.9%, which is higher than those of rare earths modified AP65 (64.1%) [1], AZ81-3Sm (57.4%) [8], T6 treated Mg-Gd-Zn (54.3%) [7], and a large number of commercial magnesium alloys such as E21, WE43, AM50, and ZE41 [32] (Table 4). As the Mg-air batteries are mainly used for low-power and long-term devices, capacity and efficiency are two of the most critical parameters for the anodes. In addition to the lower rate of gas evolution, the alleviated chunk effect of SPS also contributes to its enhanced anodic efficiencies and capacities. This viewpoint is confirmed by the corroded electrode surfaces after cleaning the oxidation products. According to Fig. 7(a) and (c), H suffers filiform corrosion with abundant grooves on its surfaces when discharged at 10 and 20 mA cm^{-2} for 10 min, respectively. The magnified images suggest the angular grooves (Fig. 7(b) and (d)) and hence indicate the shedding of metallic particles during the initial discharge. This result finally causes severe chunk effect as the discharge period prolongs to 10 h, leaving the uneven surfaces of H after removing the oxidation products (Fig. 8(a) and (c)). In addition, different grains in H have different directions of grooves, which are separated by grain boundaries (Fig. 7(a) and (c)) because of the varied crystallographic orientations [33]. Hydrogen is reported to evolve near or at the leading edges of propagated grooves [34] and thus debases the anodic efficiencies and capacities of H.

[Insert Table 4 here]

[Insert Fig. 7 here]

[Insert Fig. 8 here]

In contrast, SPS exhibits different dissolution behaviour without any filiform corrosion during the initial discharge, as affirmed by Fig. 7(e) and (g). The magnified images shown in Fig. 7(f) and (h) manifest that SPS undergoes active dissolution and the angular pits are less obvious than those of H. This phenomenon induces the relatively even surfaces discharged for 10 h (Fig. 8(e) and (g)). The three-dimensional morphologies given in Fig. 9 clearly reveal the surface roughness after long period of discharge. Increasing the current density decreases the surface roughness for both samples, while SPS displays smaller roughness than H at each current density. Therefore, uniform dissolution is achieved for SPS when applied anodic current and the chunk effect could be suppressed to some degree, leading to its higher anodic efficiencies and capacities during battery discharge. According to Fig. 7(f) and (h), SPS consists of numerous metallic particles, which are produced via ball milling (SEM image in Fig. 1) and firmly sintered together. These micron-scale particles consist of ultrafine grains that exert a vital effect on controlling the discharge and corrosion behaviour of magnesium anode. Uniform and active dissolution with mitigated side hydrogen evolution is achieved benefiting from the ultrafine grains, therefore contributing to an enhancement of anode performance for AZ31 magnesium alloy.

[Insert Fig. 9 here]

4. Conclusions

The AZ31 magnesium anode with ultrafine grains (667.28 ± 291.35 nm) is prepared via spark plasma sintering of the alloy powder that has been treated by employing high-energy ball milling.

Akin to the precursor AZ31 with the average grain size of 472.89 ± 154.31 μm, the ultrafine-grained AZ31 also exhibits low dislocation density, weak grain orientation, and dispersed nano-scale Al_3Mn phase. This modified AZ31 is adopted as the anode of Mg-air battery for the first time; its discharge and corrosion behaviour is in comparison with that of precursor AZ31 anode. The main conclusions are drawn as follows:

(i) The precursor AZ31 with micron-scale grains has strong corrosion resistance at OCP due to the protective surface film. However, it displays weak activity during the discharge of Mg-air battery and suffers filiform corrosion that promotes severe side hydrogen evolution and chunk effect with prolonged period. All these results could reflect the poor anode performance of the precursor AZ31 magnesium alloy.

(ii) The ultrafine grains in the modified AZ31 accelerate the dissolution of surface oxide film and cause the weak corrosion resistance at OCP. However, the anodic kinetics is greatly boosted and the oxidation products are removed quickly via self-peeling during battery discharge. Moreover, the modified AZ31 undergoes uniform dissolution with alleviated chunk effect; no filiform corrosion is observed when applied anodic current and the parasitic hydrogen evolution is effectively inhibited.

(iii) The desirable anode performance of the modified AZ31 is attributed to its ultrafine grains that create obviously more grain boundaries than the precursor AZ31 with micro-scale grains. The grain boundaries with higher energy serve as the local anodic regions, while the intragranular areas act as the local cathodes due to their lower energy. Consequently, the smaller ratio of local cathodes/ anodes is established in the ultrafine-grained AZ31, giving rise to its stronger activity and inhibited the side hydrogen evolution during battery discharge.

(iv) The Mg-air battery adopting the ultrafine-grained AZ31 anode provides a high voltage of

1.211 ± 0.004 V at 10 mA cm^{-2}. Its capacity at this current density reaches 1530 ± 20 mA h g^{-1} and the corresponding efficiency is 69.1 ± 0.9%, which is higher than those of rare earths modified AP65 (64.1%) and a large number of commercial magnesium alloys. Hence, constructing the magnesium alloy with ultrafine grains, low dislocation density, and weak grain orientation would enlighten the fabrication of high-performance anodes for Mg-air batteries. For further modification, it would be worth investigating the addition of several elements to the ultrafine-grained AZ31 for enhancing its corrosion resistance at OCP without the loss of discharge activity.

Acknowledgements

This work is supported by the National Nature Science Foundation of China (51401243) and the Department of Science and Technology of Guangdong Province, China (2019A050510043).

References

[1] N. Wang, W. Li, Y. Huang, G. Wu, M. Hu, G. Li, Z. Shi, Wrought Mg-Al-Pb-RE alloy strips as the anodes for Mg-air batteries, J. Power Sources, 436 (2019) 226855.

[2] X. Liu, J. Xue, P. Zhang, Z. Wang, Effects of the combinative Ca, Sm and La additions on the electrochemical behaviors and discharge performance of the as-extruded AZ91 anodes for Mg-air batteries, J. Power Sources, 414 (2019) 174-182.

[3] J. Li, Q. Jiang, H. Sun, Y. Li, Effect of heat treatment on corrosion behavior of AZ63 magnesium alloy in 3.5 wt.% sodium chloride solution, Corros. Sci., 111 (2016) 288-301.

[4] W. Zhang, Q. Liu, Y. Chen, G. Wan, Anodic dissolution dictates the negative difference effect (NDE) of magnesium corrosion more in chemical pathway, Mater. Lett., 232 (2018) 54-57.

[5] N. Wang, R. Wang, C. Peng, B. Peng, Y. Feng, C. Hu, Discharge behaviour of Mg-Al-Pb and Mg-Al-Pb-In alloys as anodes for Mg-air battery, Electrochim. Acta, 149 (2014) 193-205.

[6] J. Li, Z. Chen, J. Jing, J. Hou, Electrochemical behavior of Mg-Al-Zn-Ga-In alloy as the anode for seawater-activated battery, J. Mater. Sci. Technol., 41 (2020) 33-42.

[7] X. Chen, H. Wang, Q. Zou, Q. Le, C. Wen, A. Atrens, The influence of heat treatment on discharge and electrochemical properties of Mg-Gd-Zn magnesium anode with long period stacking ordered structure for Mg-air battery, Electrochim. Acta, 367 (2021) 137518.

[8] X. Chen, Q. Liao, Q. Le, Q. Zou, H. Wang, A. Atrens, The influence of samarium (Sm) on the discharge and electrochemical behaviors of the magnesium alloy AZ80 as an anode for the Mg-air battery, Electrochim. Acta, 348 (2020) 136315.

[9] X. Liu, S. Liu, J. Xue, Discharge performance of the magnesium anodes with different phase constitutions for Mg-air batteries, J. Power Sources, 396 (2018) 667-674.

[10] Q. Cui, D. Yi, H. Wang, J. Zhang, J. Xu, B. Wang, Effects of grain size and secondary phase on corrosion behavior and electrochemical performance of Mg-3Al-5Pb-1Ga-Y sacrificial anode, J. Rare Earths, 37 (2019) 1341-1350.

[11] G.-L. Song, Z. Xu, Effect of microstructure evolution on corrosion of different crystal surfaces of AZ31 Mg alloy in a chloride containing solution, Corros. Sci., 54 (2012) 97-105.

[12] T. Zheng, Y. Hu, S. Yang, Effect of grain size on the electrochemical behavior of pure magnesium anode, J. Magnes. Alloy, 5 (2017) 404-411.

[13] X. Liu, Z. Guo, J. Xue, P. Zhang, The role of Al_2Ca and Al_2(Sm,Ca,La) particles in the microstructures and electrochemical discharge performance of as-extruded Mg-3wt.%Al-1wt.%Zn-based alloys for primary Mg-air batteries, Int. J. Energy Res., 43 (2019) 4569-4579.

[14] D. Song, A. Ma, J. Jiang, P. Lin, D. Yang, J. Fan, Corrosion behavior of equal-channel-angular-pressed pure magnesium in NaCl aqueous solution, Corros. Sci., 52 (2010) 481-490.

[15] B.J. Wang, D.K. Xu, J.H. Dong, W. Ke, Effect of the crystallographic orientation and twinning on the corrosion resistance of an as-extruded Mg–3Al–1Zn (wt.%) bar, Scr. Mater., 88 (2014) 5-8.

[16] A. Henaish, Physical and spectral studies of Mg-Zn ferrite prepared by different methods, Arab J. Nucl. Sci. Appl., 53 (2019) 9-18.

[17] D. Guan, W.M. Rainforth, J. Sharp, J. Gao, I. Todd, On the use of cryomilling and spark plasma sintering to achieve high strength in a magnesium alloy, J. Alloys Compd., 688 (2016) 1141-1150.

[18] Y. Luo, Y. Wu, Q. Deng, Y. Zhang, J. Chen, L. Peng, Microstructures and mechanical properties of Mg-Gd-Zn-Zr alloys prepared by spark plasma sintering, J. Alloys Compd., 820 (2020) 153405.

[19] N. Saikrishna, G. Pradeep Kumar Reddy, B. Munirathinam, B. Ratna Sunil, Influence of bimodal grain size distribution on the corrosion behavior of friction stir processed biodegradable AZ31 magnesium alloy, J. Magnes. Alloy, 4 (2016) 68-76.

[20] R.B. Figueiredo, T.G. Langdon, Analysis of the creep behavior of fine-grained AZ31 magnesium alloy, Mater. Sci. Eng., A, 787 (2020) 139489.

[21] H.S. Kim, G.H. Kim, H. Kim, W.J. Kim, Enhanced corrosion resistance of high strength Mg–3Al–1Zn alloy sheets with ultrafine grains in a phosphate-buffered saline solution, Corros. Sci., 74 (2013) 139-148.

[22] H.J. Choi, Y. Kim, J.H. Shin, D.H. Bae, Deformation behavior of magnesium in the grain size spectrum from nano- to micrometer, Mater. Sci. Eng., A, 527 (2010) 1565-1570.

[23] L. Fan, H. Lu, The effect of grain size on aluminum anodes for Al–air batteries in alkaline electrolytes, J. Power Sources, 284 (2015) 409-415.

[24] H. Yang, L. Wu, B. Jiang, W. Liu, J. Song, G. Huang, D. Zhang, F. Pan, Clarifying the roles of grain boundary and grain orientation on the corrosion and discharge processes of α-Mg based Mg-Li alloys for primary Mg-air batteries, J. Mater. Sci. Technol., 62 (2021) 128-138.

[25] K.R. Kim, J.W. Ahn, G.-H. Kim, J.H. Han, K.K. Cho, J.-S. Roh, W.J. Kim, H.S. Kim, Corrosion behavior of magnesium powder fabricated by high-energy ball milling and spark plasma sintering, Met. Mater. Int., 20 (2014) 1095-1101.

[26] G.-L. Song, Z. Shi, Corrosion mechanism and evaluation of anodized magnesium alloys, Corros. Sci., 85 (2014) 126-140.

[27] M. Alvarez-Lopez, M.D. Pereda, J.A. del Valle, M. Fernandez-Lorenzo, M.C. Garcia-Alonso, O.A. Ruano, M.L. Escudero, Corrosion behaviour of AZ31 magnesium alloy with different grain sizes in simulated biological fluids, Acta Biomater., 6 (2010) 1763-1771.

[28] Z. Cui, X. Li, K. Xiao, C. Dong, Atmospheric corrosion of field-exposed AZ31 magnesium in a tropical marine environment, Corros. Sci., 76 (2013) 243-256.

[29] E.V. Parfenov, O.B. Kulyasova, V.R. Mukaeva, B. Mingo, R.G. Farrakhov, Y.V. Cherneikina, A. Yerokhin, Y.F. Zheng, R.Z. Valiev, Influence of ultra-fine grain structure on corrosion behaviour of biodegradable Mg-1Ca alloy, Corros. Sci., 163 (2020) 108303.

[30] A. Bahmani, S. Arthanari, K.S. Shin, Formulation of corrosion rate of magnesium alloys using microstructural parameters, J. Magnes. Alloy, 8 (2020) 134-149.

[31] C.Q. Li, D.K. Xu, Z.R. Zhang, E.H. Han, Influence of the lithium content on the negative difference effect of Mg-Li alloys, J. Mater. Sci. Technol., 57 (2020) 138-145.

[32] M. Deng, L. Wang, D. Höche, S.V. Lamaka, D. Snihirova, B. Vaghefinazari, M.L. Zheludkevich, Clarifying the decisive factors for utilization efficiency of Mg anodes for primary aqueous batteries, J. Power Sources, 441 (2019) 227201.

[33] G.-L. Song, Z. Xu, Crystal orientation and electrochemical corrosion of polycrystalline Mg, Corros. Sci., 63 (2012) 100-112.

[34] S. Fajardo, G.S. Frankel, Effect of impurities on the enhanced catalytic activity for hydrogen evolution in high purity magnesium, Electrochim. Acta, 165 (2015) 255-267.

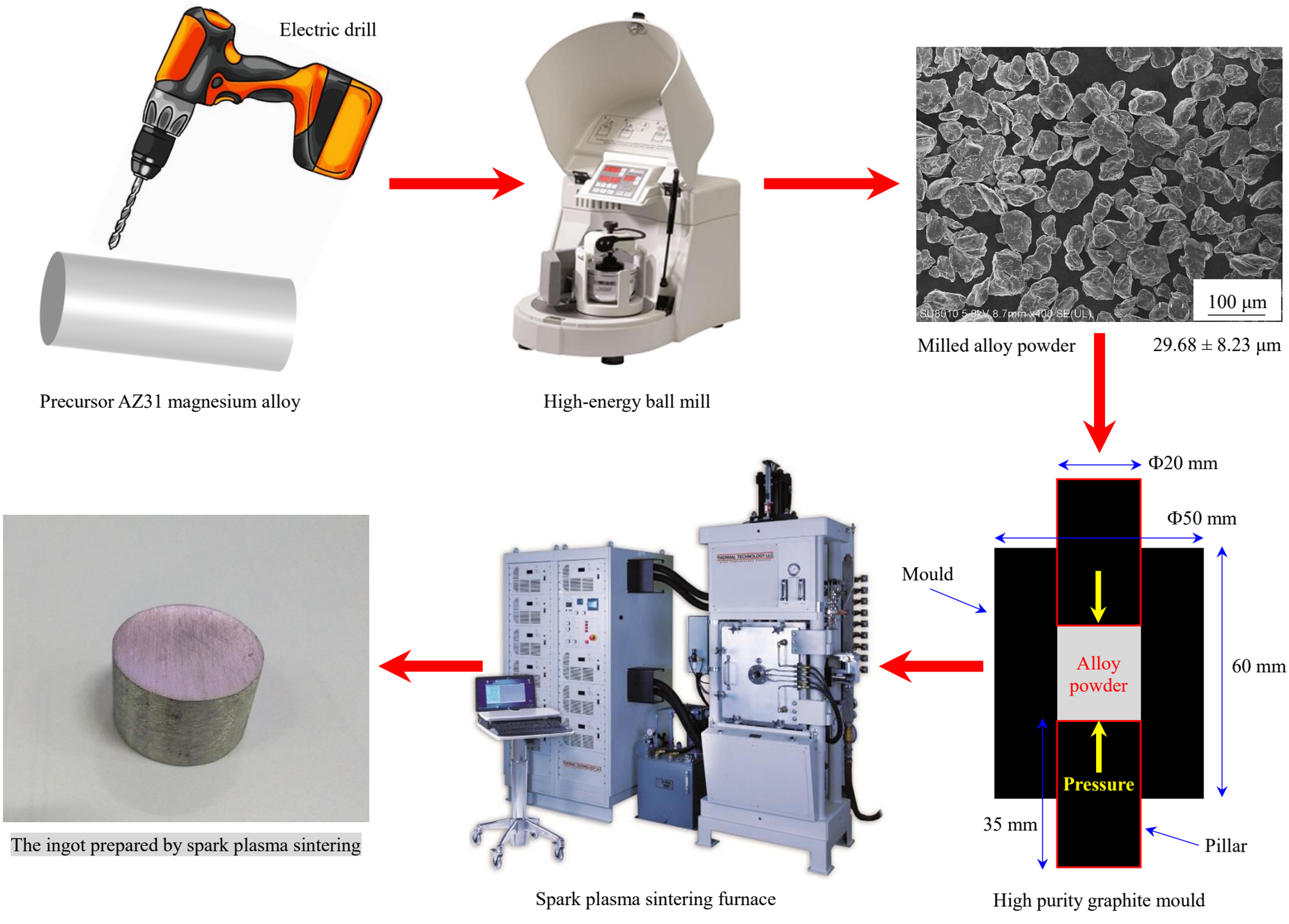

Fig. 1 Schematics of synthesizing AZ31 magnesium anode via ball milling and spark plasma sintering. The drill cuttings of precursor AZ31 are obtained in the glovebox by using an electric drill and then subjected to high-energy ball milling to prepare the alloy powder, which is sintered via spark plasma sintering to fabricate the bulk magnesium alloy.

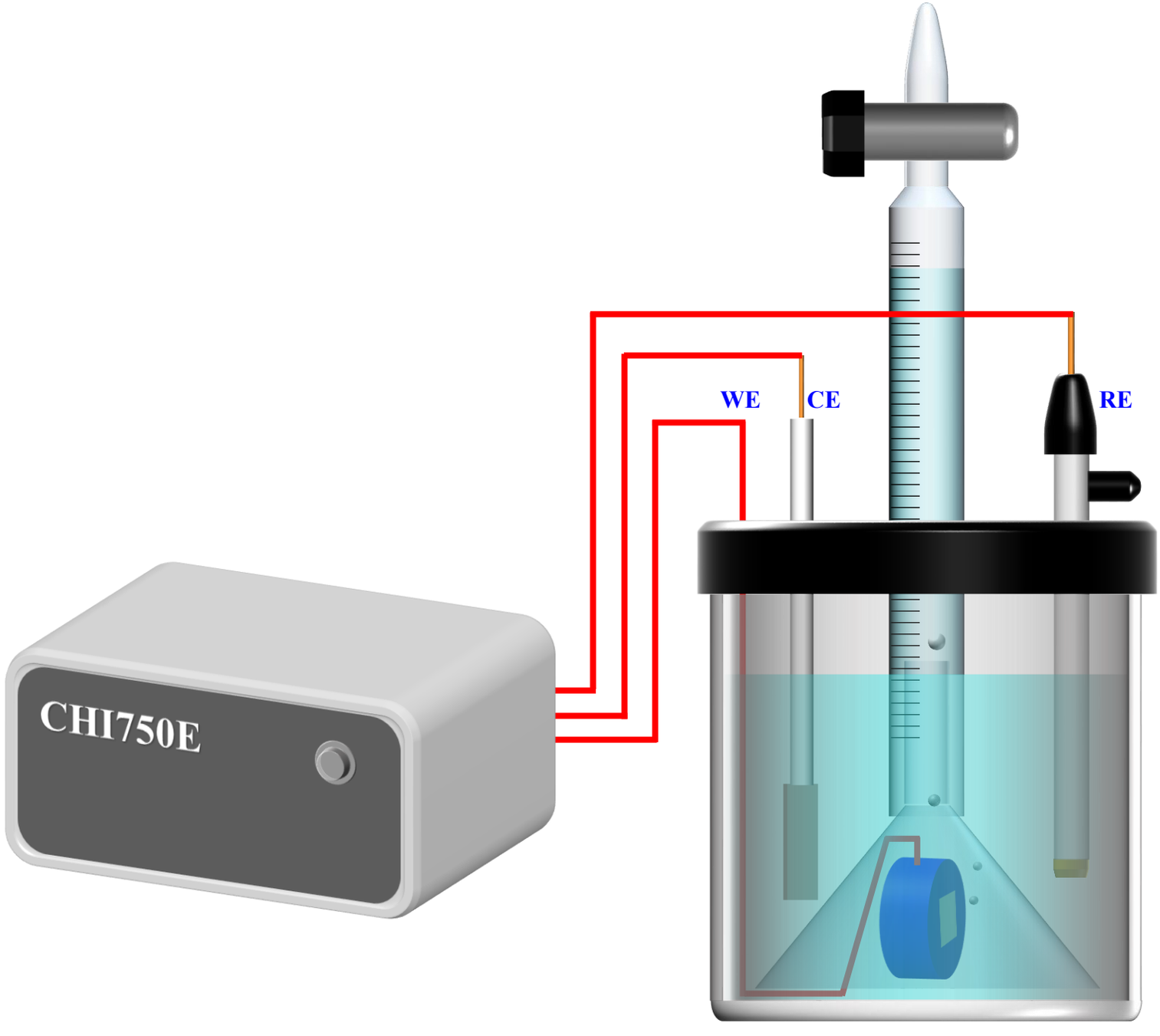

Fig. 2 Schematics of measuring the volume of hydrogen during galvanostatic discharge. WE is working electrode, CE is counter electrode, and RE is reference electrode.

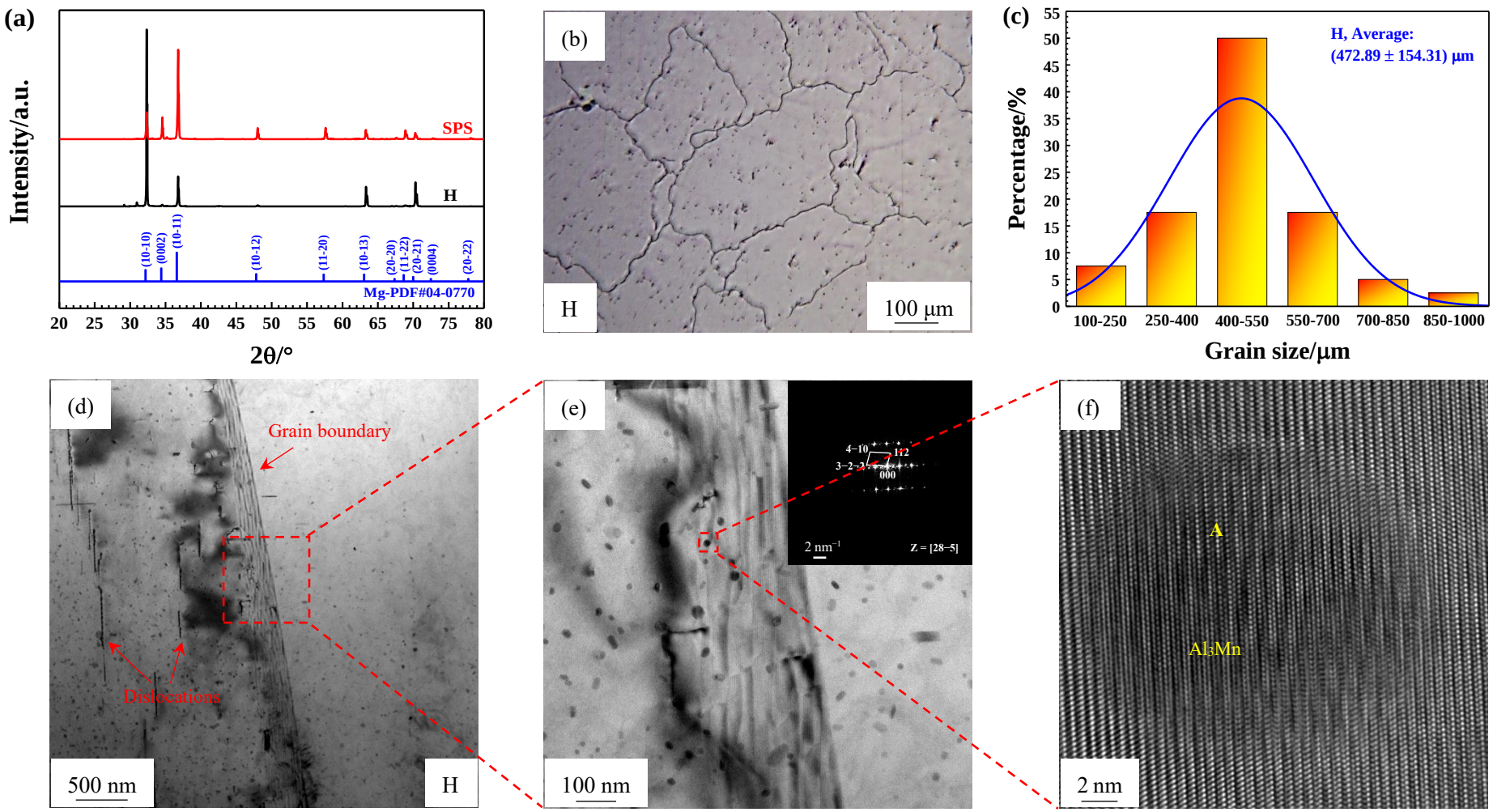
(a)
Intensity/a.u.
SPS
H
(10-10)
(0002)
(10-11)
(10-12)
(11-20)
(10-13)
(20-20)
(11-22)
(20-21)
(0004)
(20-22)
Mg-PDF#04-0770
20 25 30 35 40 45 50 55 60 65 70 75 80
2θ/°
(b)
H
100 μm
(c)
H, Average:
(472.89 ± 154.31) μm
Percentage/%
0 5 10 15 20 25 30 35 40 45 50 55
100-250 250-400 400-550 550-700 700-850 850-1000
Grain size/μm
(d)
Grain boundary
Dislocations
500 nm
H
(e)
4−10
1̄12
3−2−3
000
2 nm⁻¹
Z = [28−5]
100 nm
(f)
A
Al3Mn
2 nm

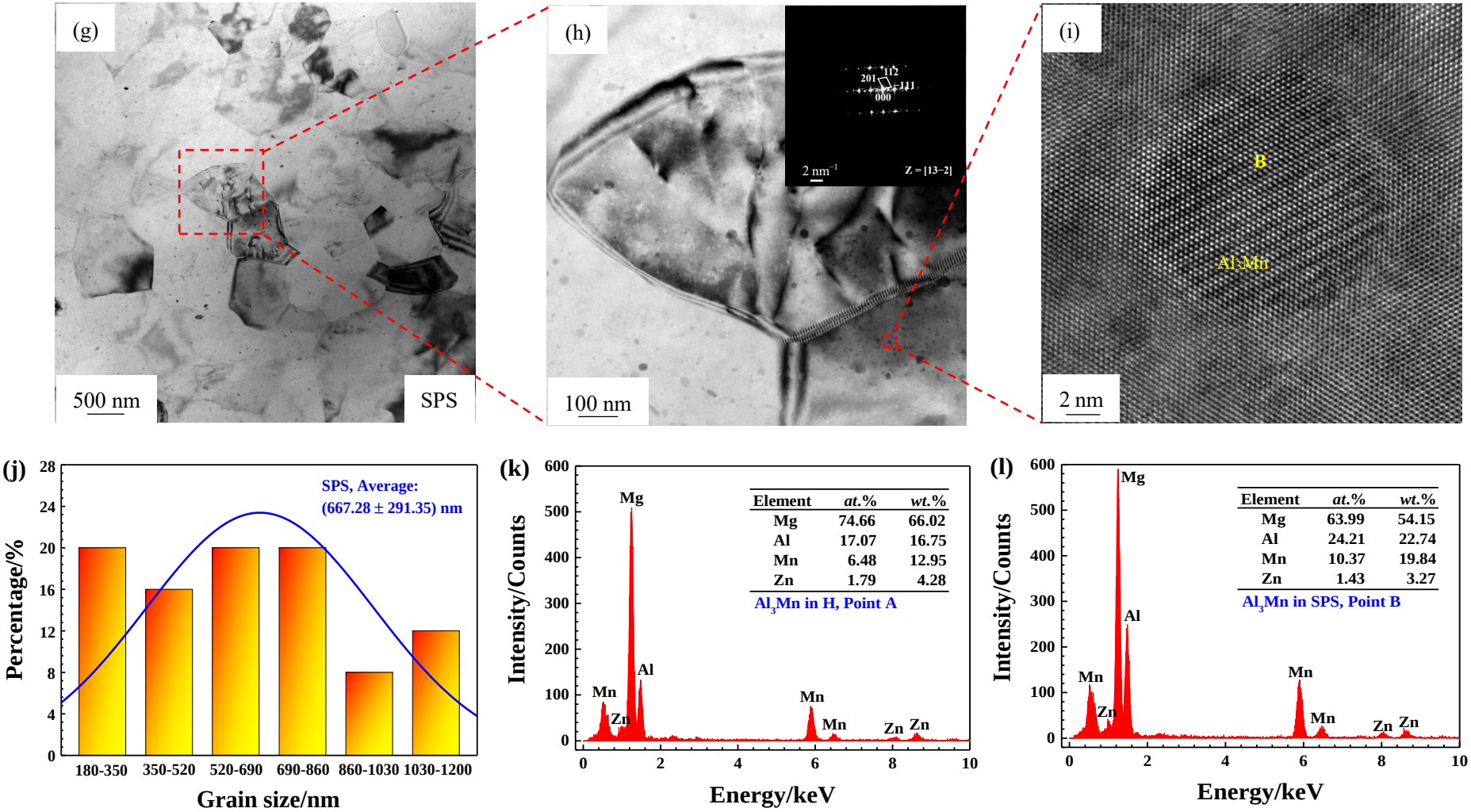

Fig. 3 (a) XRD spectra, (b) Optical micrograph of H, (c) Grain size distribution of H, (d)-(f) TEM images of H, (g)-(i) TEM images of SPS, (j) Grain size distribution of SPS, (k) EDX analysis of Point A in Fig. 2(f), and (l) EDX analysis of Point B in Fig. 2(i). The inserted figures shown in Fig. 2(e) and (h) are the FFT results according to the HR-TEM images given in Fig. 2(f) and (i), respectively.

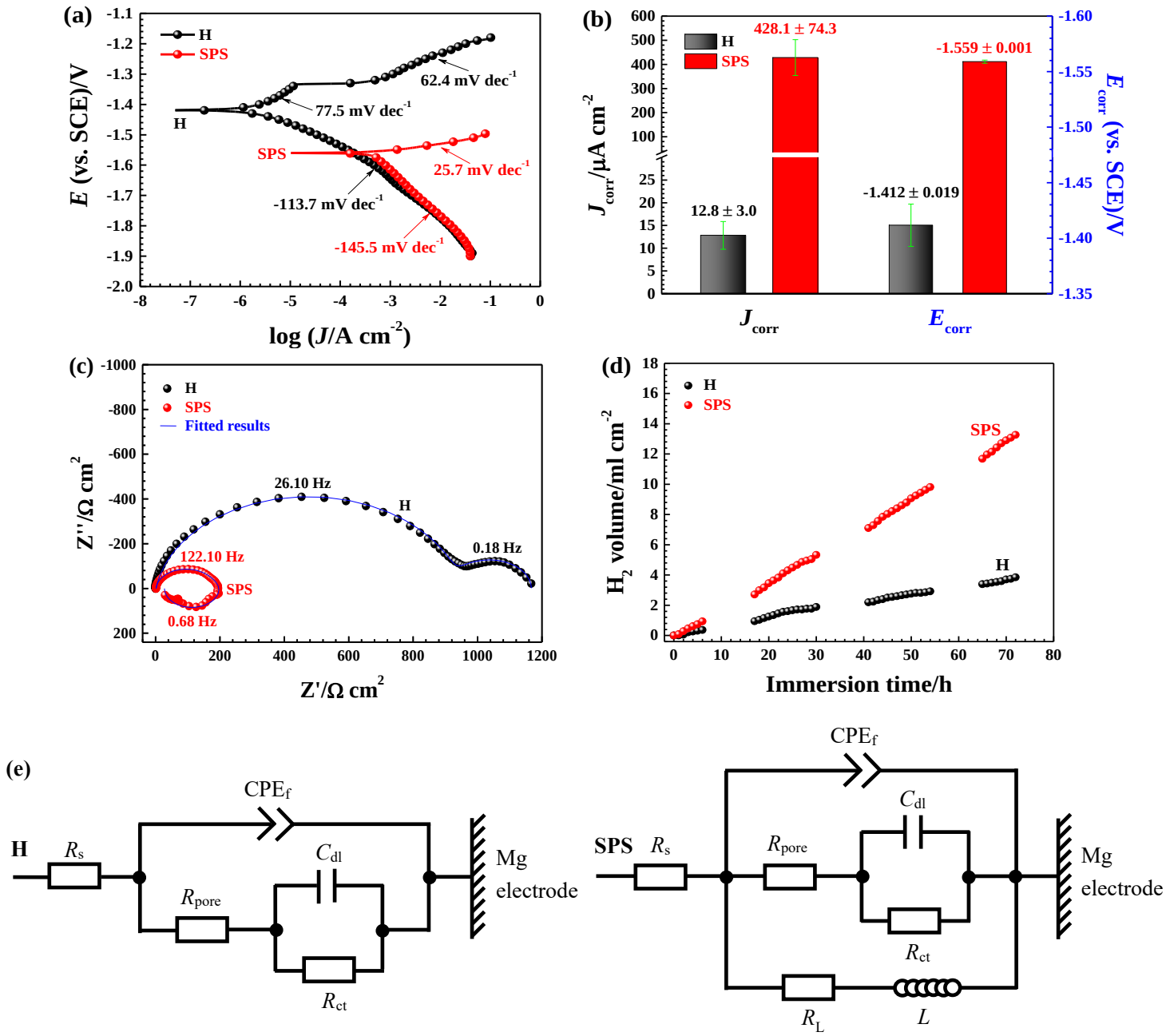

Fig. 4 (a) Polarization curves, (b) Corrosion current densities (J_{corr}) and Corrosion potentials (E_{corr}), (c) EIS at OCPs, (d) Hydrogen evolution behaviour at OCPs, and (e) Equivalent circuits for fitting the EIS. The electrolyte is 3.5 wt.% NaCl aqueous solution. In the equivalent circuits, R_s is the solution resistance, R_{pore} is the resistance for electrolyte ions penetrating through the pores of surface film, R_{ct} is the charge transfer resistance, L is the inductance, CPE_f is the constant phase elements of the surface film, and C_{dl} is the capacitance of electric double layer.

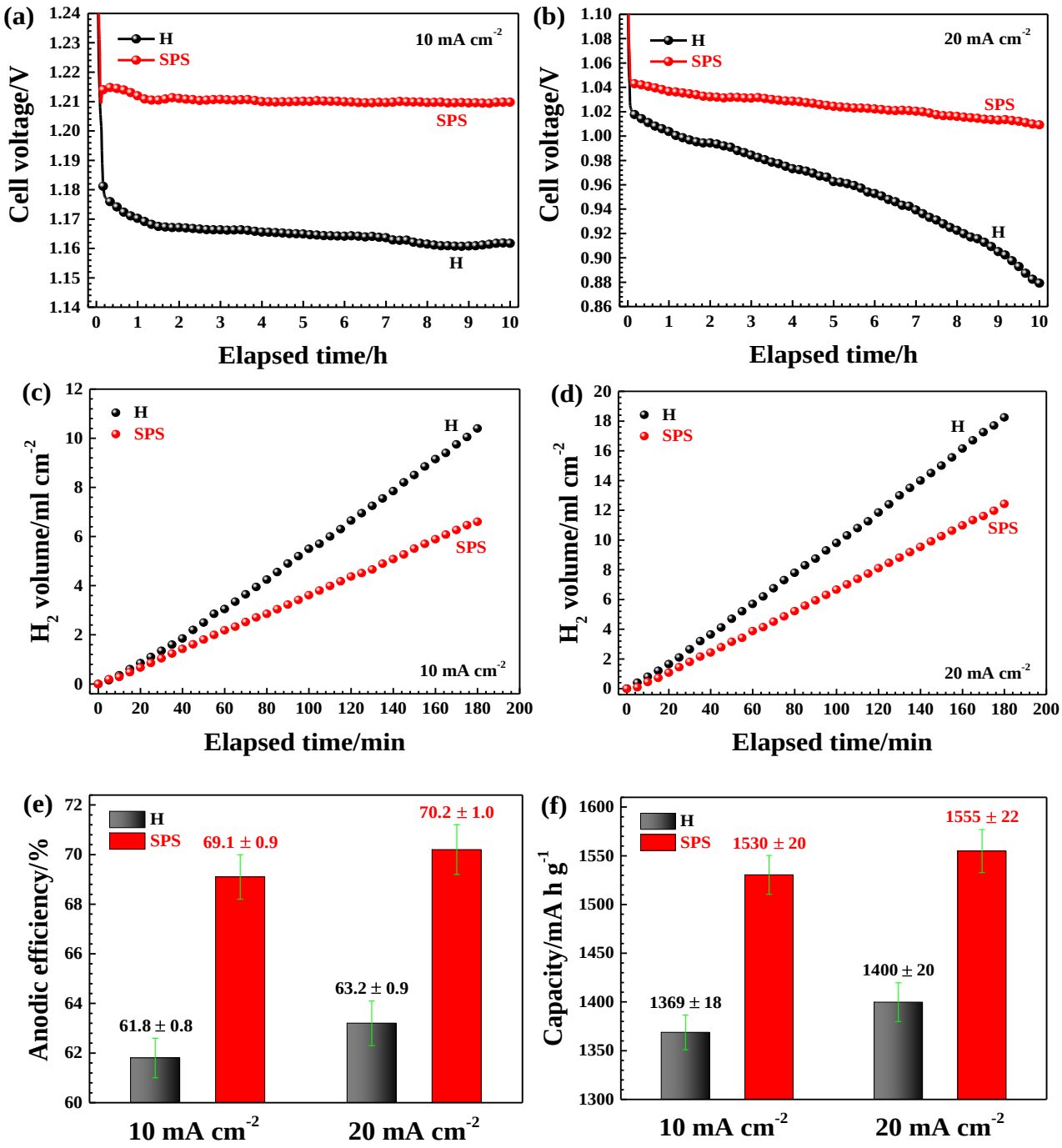

Fig. 5 Voltage-time curves of Mg-air batteries at (a) 10 mA cm^{-2} and (b) 20 mA cm^{-2}, Hydrogen evolution behaviour at (c) 10 mA cm^{-2} and (d) 20 mA cm^{-2}, (e) Anodic efficiencies and (f) Capacities during galvanostatic discharge for 10 h. The electrolyte is 3.5 wt.% NaCl aqueous solution and the cathode catalyst is commercial MnO_2/C hybrid.

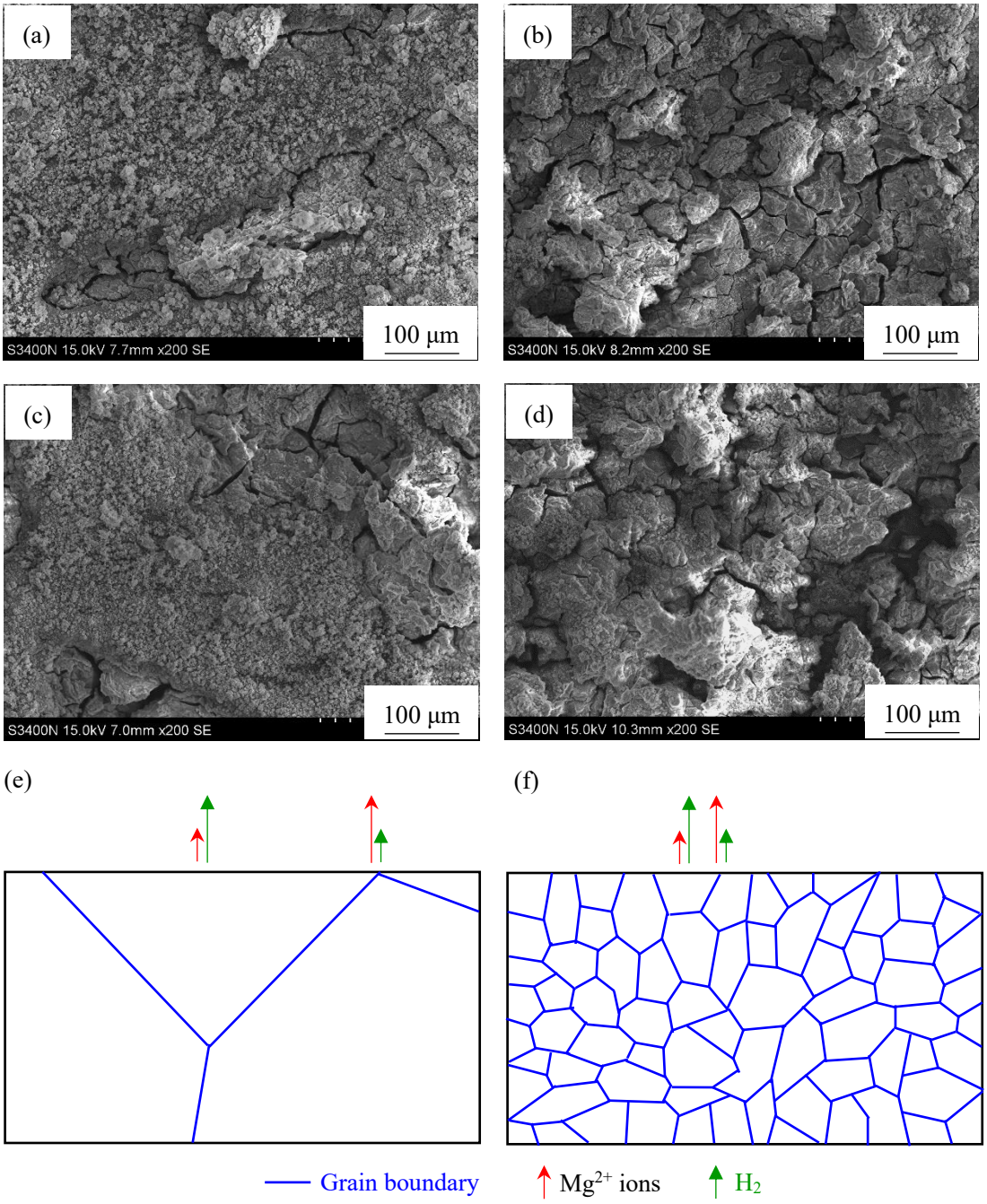

Fig. 6 Surface morphologies after battery discharge for 1 h without removing the oxidation products: (a) H at 10 mA cm^{-2}, (b) SPS at 10 mA cm^{-2}, (c) H at 10 mA cm^{-2}, and (d) SPS at 10 mA cm^{-2}. Schematics for illustrating the anodic dissolution and hydrogen evolution of magnesium electrodes during battery discharge: (e) H and (f) SPS.

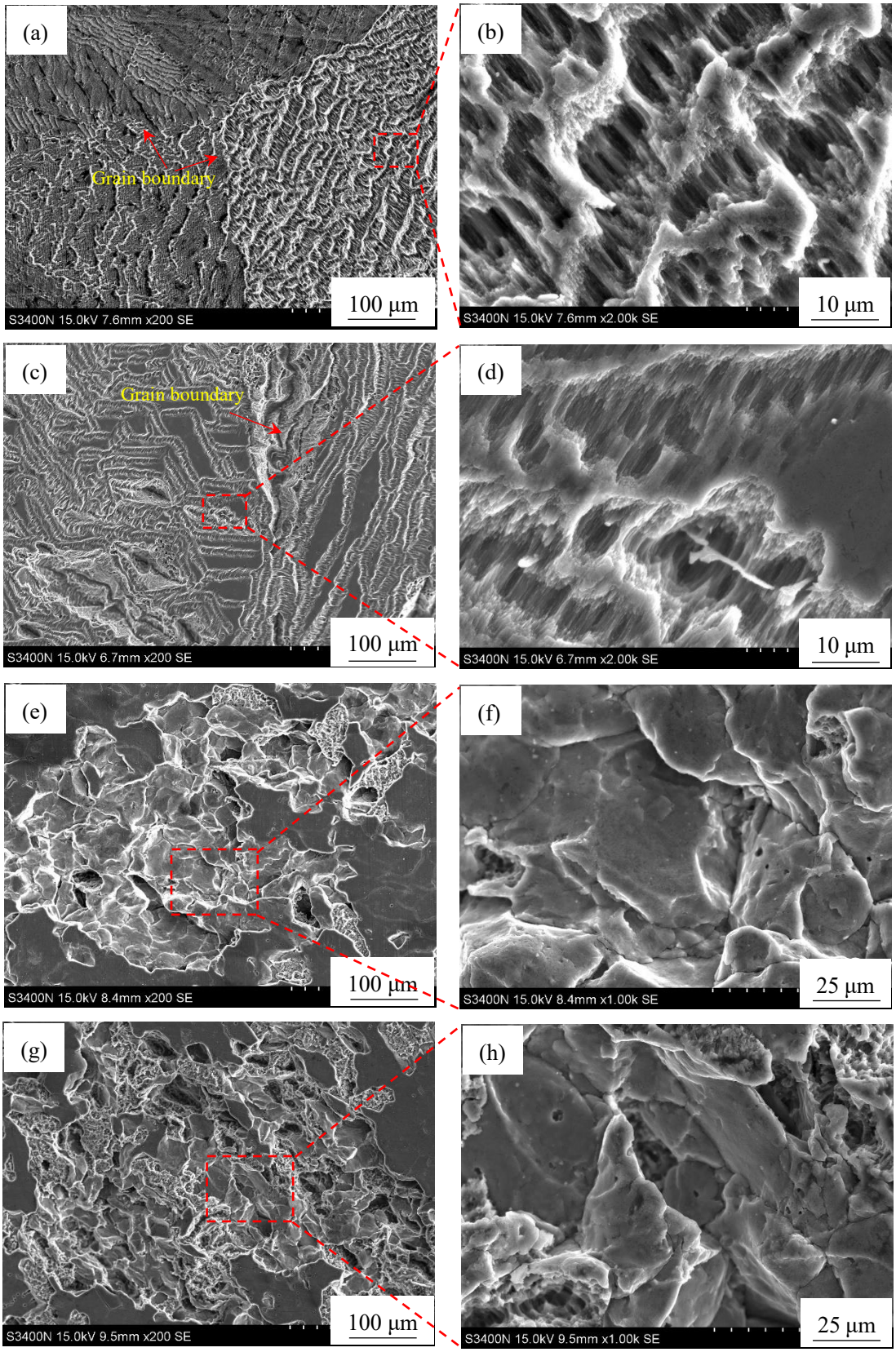

Fig. 7 Surface morphologies discharged for 10 min after removing the oxidation products: (a)-(b) H at 10 mA cm^{-2}, (c)-(d) H at 20 mA cm^{-2}, (e)-(f) SPS at 10 mA cm^{-2}, and (g)-(h) SPS at 20 mA cm^{-2}.

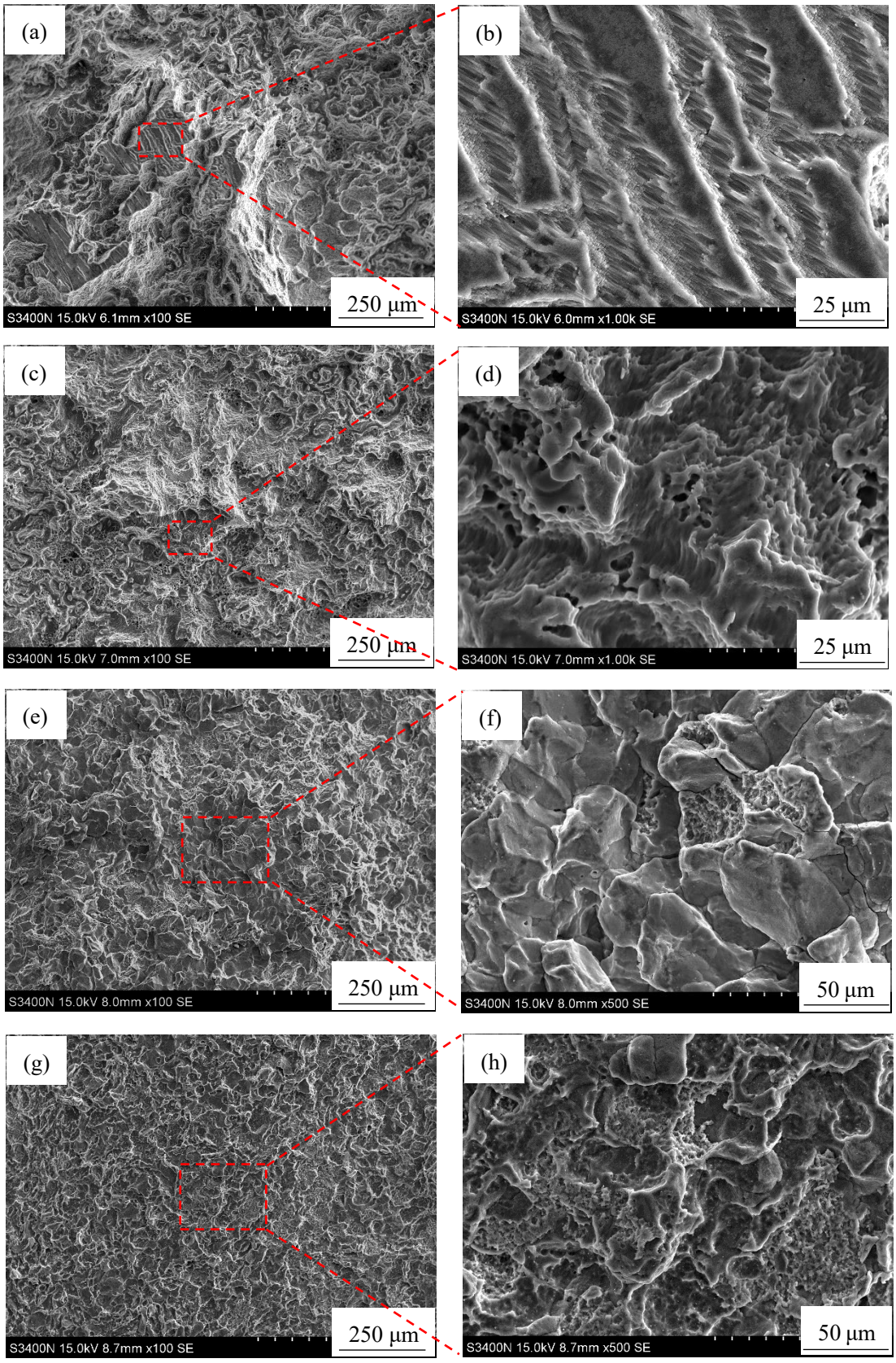

Fig. 8 Surface morphologies discharged for 10 h after removing the oxidation products: (a)-(b) H at 10 mA cm^{-2}, (c)-(d) H at 20 mA cm^{-2}, (e)-(f) SPS at 10 mA cm^{-2}, and (g)-(h) SPS at 20 mA cm^{-2}.

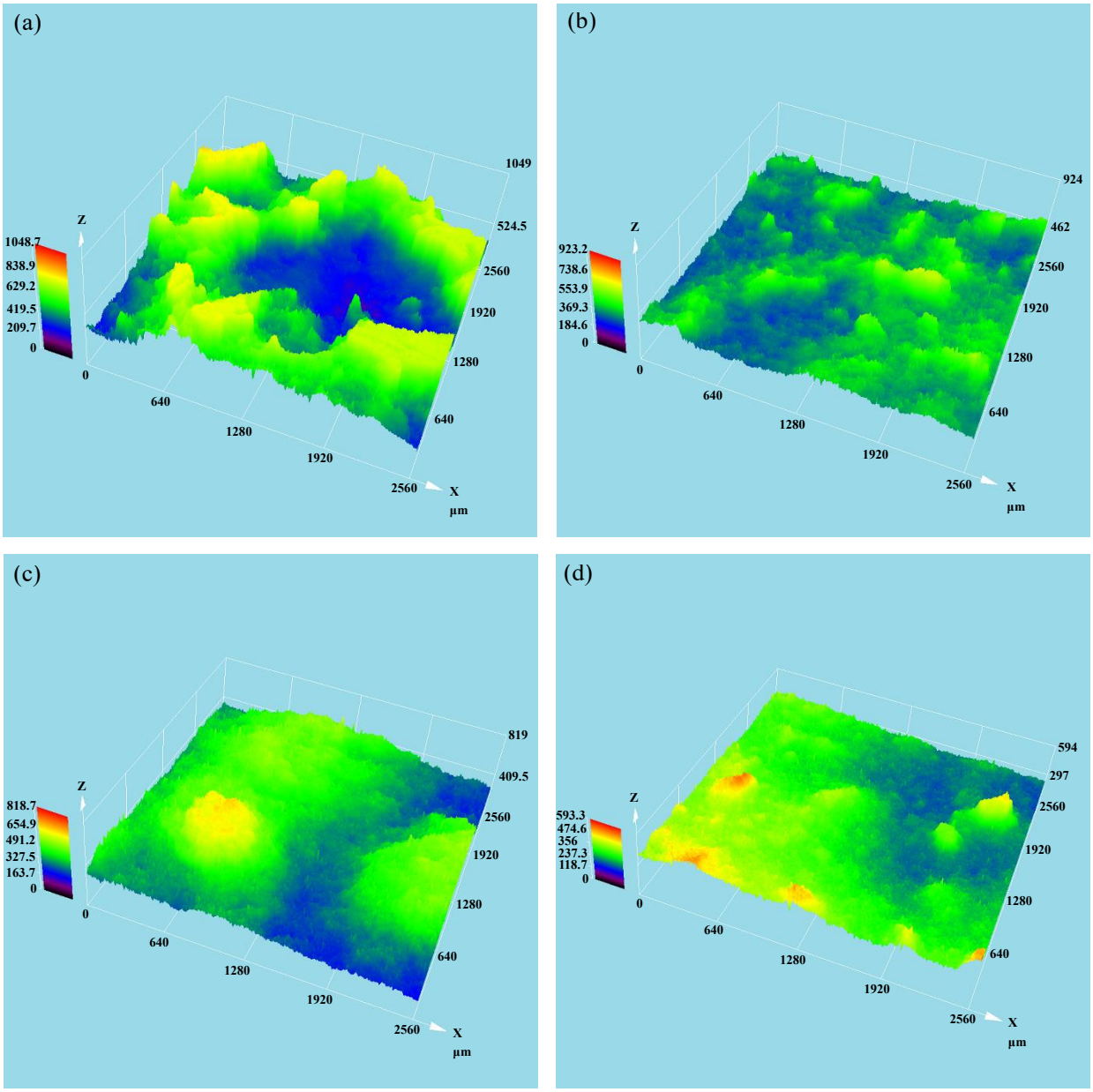

Fig. 9 Three-dimensional surface morphologies discharged for 10 h after removing the oxidation products: (a) H at 10 mA cm^{-2}, (b) H at 20 mA cm^{-2}, (c) SPS at 10 mA cm^{-2}, and (d) SPS at 20 mA cm^{-2}.

Table 1 Electrochemical parameters based on the fitting of EIS at OCPs

Mg electrode	R_s/(Ω cm^2)	R_{pore}/(Ω cm^2)	Y_f/(Ω^{-1} cm^{-2} s^n)	n_f	R_{ct}/(Ω cm^2)	C_{dl}/(Ω^{-1} cm^{-2} s)
H	2	945	1.1×10^{-5}	0.91	220	3.0×10^{-3}
SPS	2	185	9.0×10^{-6}	0.955	11	7.0×10^{-4}

Mg electrode	R_L/(Ω cm^2)	L/(H cm^2)	χ^2
H	–	–	3.1×10^{-4}
SPS	30	80	3.6×10^{-4}

Y_f is the parameter akin to the capacitance and n_f is an index without dimension.

Table 2 Average voltages during the discharge of 10 h at different current densities

Average voltage/V	10 mA cm^{-2}	20 mA cm^{-2}
H	1.166 ± 0.005	0.959 ± 0.008
SPS	1.211 ± 0.004	1.026 ± 0.007

Table 3 Hydrogen evolution rates (V_H) under different conditions

V_H/(ml cm^{-2} h^{-1})	OCP for 72 h	10 mA cm^{-2} for 3 h	20 mA cm^{-2} for 3 h
H	0.05 ± 0.01	3.47 ± 0.06	6.08 ± 0.08
SPS	0.18 ± 0.02	2.20 ± 0.05	4.14 ± 0.08

Table 4 Literature survey for anodic efficiencies of several magnesium anodes at 10 cm^{-2}

Magnesium anode	Anodic efficiency/%	Reference
Rare earths modified AP65	64.1	*J. Power Sources*, 2019, 436: 226855
AZ81-3Sm	57.4	*Electrochim. Acta*, 2020, 348: 136315
T6 treated Mg-Gd-Zn	54.3	*Electrochim. Acta*, 2021, 367: 137518
E21	45.1	*J. Power Sources*, 2019, 441: 227201
WE43	50.0	*J. Power Sources*, 2019, 441: 227201
AM50	43.2	*J. Power Sources*, 2019, 441: 227201
ZE41	31.0	*J. Power Sources*, 2019, 441: 227201
H	61.8	This work
SPS	69.1	This work

*The electrolyte is 3.5 wt.% NaCl aqueous solution.